Inorganic Chemistry

ARTICLE

pubs.acs.org/IC

Emissive Iridium(III) Diimine Complexes Formed by Double Cyclometalation of Coordinated Triphenylphosphite

Yao-Yuan Chang,[†] Jui-Yi Hung,[†] Yun Chi,*[,†] Jong-Pyng Chyn,[‡] Min-Wen Chung,[§] Chia-Li Lin,[§] Pi-Tai Chou,*[,§] Gene-Hsiang Lee,[§] Chih-Hao Chang,*[,⊥] and Wei-Chieh Lin[⊥]

[†]Department of Chemistry, National Tsing Hua University, Hsinchu 30013, Taiwan

[‡]Department of Chemistry, R. O. C. Military Academy, Fengshan 830, Taiwan

[§]Department of Chemistry, National Taiwan University, Taipei 10617, Taiwan

[⊥]Department of Photonics Engineering, Yuan Ze University, Chung-Li 32003, Taiwan

Supporting Information

ABSTRACT: We report on the synthesis of a new series of iridium(III) complexes functionalized with various diimine chromophores, together with a *facially* coordinated dicyclometalated phosphite chelate and a monodentate anionic ancillary. This conceptual design presents a novel strategy in obtaining a new class of iridium(III) diimine complexes without employment of traditional nitrogen-containing polyaromatic cyclometalates. Additionally, we discuss the basic charactersistics of the ground and lower-lying excited states involved, as documented by crystal structural, photophysical studies, and density functional theory calculations. Fabrication of the green-emitting organic light-emitting diodes with one such dopant, [Ir(dbbpy)(tpit)NCS] (**2b**), where dbbpy and tpit represent di-*tert*-butyl-2,2′-bipyridine and dicyclometalated triphenylphosphite, respectively, was successfully made, attaining a peak external quantum efficiency (η_{ext}), a luminance efficiency (η_l), and a power efficiency (η_p) of 14.1%, 46.6 cd A^{-1}, and 39.9 lm W^{-1}, respectively.

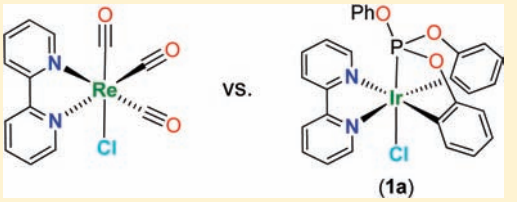

INTRODUCTION

Late-transition-metal and third-row transition-metal complexes with diimine ligands such as 2,2′-bipyridine or functionalized entities have attracted great interest because of their applications in materials chemistry, metal catalysts, and optoelectronics.[1] Their characteristic robustness and higher luminescent efficiencies also make them excellent candidates as a paradigm for probing the basic coordination chemistry and the associated catalytic and photophysical properties. Particularly, the diimine metal complexes with d^6 electronic configuration are ubiquitous because of their greater thermal stability, higher luminescent efficiency, and versatility to which the electronic properties of the ligands can be tuned.[2] Recently, studies are also extended to the whole series of d^6 metal complexes, i.e., those with W^0, Re^I, Os^{II}, and Ir^{III} elements. Particularly, the boom of research on osmium(II) and iridium(III) complexes is driven by the urgent need for highly efficient, phosphorescent materials for organic light-emitting diodes (OLEDs).[3]

Charge-neutral tungsten(0) complexes like class A shown in Scheme 1 are the prototype, for which the lowest-lying electronic absorption and emission spectra are attributed to the metal-to-ligand charge-transfer (MLCT) transitions and which is commonly highly solvent-dependent.[4] Next, the isoelectronic rhenium(I) complexes such as class B with a chelating 2,2′-bipyridine ligand have been assembled with one anionic halide ligand to balance the 1+ charge of the central metal ion. With the broad ability to functionalize bipyridine, it then clears the way to study their fundamental properties and use relevant rhenium(I) complexes as emissive labels, probes, and sensors.[5] Switching the metal atom from rhenium(I) to osmium(II) has intuitively led to the formation of osmium(II) diimine complexes with two terminal halides, for which complexes such as class C were readily prepared from solid-state pyrolysis of $[Os(CO)_3I_2]_2$ and diimine chelate.[6]

In sharp contrast to previously discussed group 6−8 transition-metal complexes, the iridium(III) complexes with both diimine chelate and carbonyl ancillaries are not as common.[7] Apparently, the higher oxidation state at the iridium(III) metal center would reduce the π-back-bonding to the carbonyl ligand and, consequently, destabilize this bonding interaction. This explains why only a limited number of carbonyl-containing iridium(III) metal complexes have been isolated and characterized. On the other hand, the cyclometalating chelate can be utilized to substitute carbonyl ligand in order to stabilize diimine coordination to the iridium(III) metal center, which then produced a large number of cationic complexes showing bright luminescence in a degassed solution at room temperature.[8] A representative example is given by the tris-chelated iridium(III) complexes of type D, which is typically synthesized via the treatment of dimeric $[Ir(ppy)_2(\mu\text{-}Cl)]_2$ with 2,2′-bipyridine.[9] In this contribution, we report the in situ preparation of a

Received: February 22, 2011
Published: May 04, 2011

Scheme 1. Structural Drawings of Third-Row d^6 Metal Complexes with 2,2′-Bipyridine Chelates

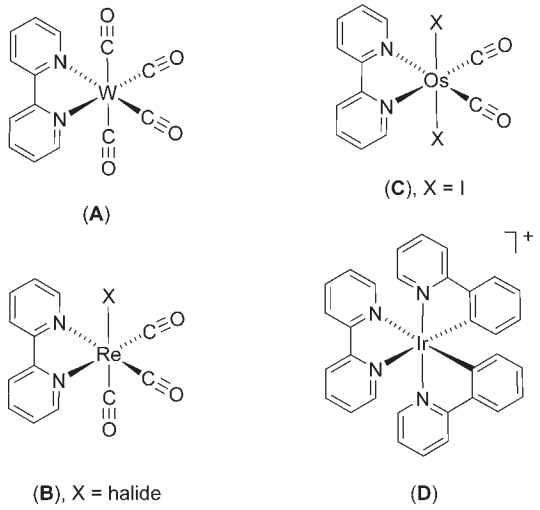

distinctively different iridium(III) diimine complex bearing *facially* coordinated, triphenylphosphite dicyclometalate, plus one terminal halide or pseudohalide ligand for maintaining the charge neutrality of the iridium(III) complex. Such a tripodal ancillary has only been isolated from either a circuitous route or the treatment of iridium(I) starting materials with hindered phosphites to promote dicyclometalation.[10] Recently, such a synthetic stalemate was finally overcome upon employment of a distinctive metal reagent $[IrCl_3(tht)_3]$, where tht = tetrahydrothiophene, which allowed the synthetic reaction to be conducted in hydrocarbon, which facilitates dicyclometalation of triphenylphosphite.[11] These new series of emissive iridium(III) complexes are then studied by absorption and emission spectroscopy together with a density functional theory (DFT) computational approach to gain insight into the relationship regarding structural versus photophysical properties. The successful fabrication of OLEDs using one of the titled complexes, [Ir(dbbpy)(tpit)NCS] (**2b**), as the dopant is also reported. Details are elaborated in the following sections.

EXPERIMENTAL SECTION

General Procedures. All reactions were performed under an argon atmosphere, and solvents were distilled from appropriate drying agents prior to use. Commercially available reagents were used without further purification unless otherwise stated. All reactions were monitored using precoated thin-layer chromatography (TLC) plates (0.20 mm with fluorescent indicator UV254). Mass spectra were obtained on a JEOL SX-102A instrument operating in electron impact (EI) or fast atom bombardment (FAB) mode. ^1H and ^{13}C NMR spectra were recorded on a Varian INOVA-500 instrument. Elemental analysis was carried out with a Heraeus CHN-O rapid elementary analyzer. Cyclic voltammetry (CV) measurements were performed using a BAS 100B/W electrochemical analyzer. For convenience, hereafter, the abbreviations for various chelates utilized in this study, i.e., 2,2′-bipyridine, di-*tert*-butyl-2,2′-bipyridine, 2,2′-biquinoline, and dicyclometalated triphenylphosphite, are defined as bpy, dbbpy, bq, and tpit, respectively.

Synthesis of 1a. $[IrCl_3(tht)_3]$ (110 mg, 0.20 mmol), $tpitH_2$ (62 mg, 0.20 mmol), bpy (31 mg, 0.20 mmol), and sodium acetate (82 mg, 1.00 mmol) were added in decalin (15 mL), and the mixture was heated to 180 °C for 8 h. After cooling to room temperature, the solvent was removed, and the residue was purified by silica gel column chromatography, eluting with a 3:1 mixture of CH_2Cl_2 and ethyl acetate. The green crystals of [Ir(bpy)(tpit)Cl] were obtained by the slow diffusion of hexane into a CH_2Cl_2 solution at room temperature (88 mg, 0.13 mmol, 64%).

Spectral Data of ***1a***. MS (FAB, ^{35}Cl, ^{193}Ir): m/z 657 $(M - Cl)^+$. ^1H NMR (500 MHz, $CDCl_3$, 294K): δ 8.18 (d, J = 7.0 Hz, 2H), 8.00 (d, J = 5.0 Hz, 2H), 7.86−7.80 (m, 4H), 7.24 (t, J = 6.0 Hz, 2H), 6.98−6.96 (m, 4H), 6.90−6.87 (m, 2H), 6.78 (t, J = 7.5 Hz, 1H), 6.61 (t, J = 8.0 Hz, 2H), 6.51 (d, J = 8.0 Hz, 2H). $^{31}P\{^1H\}$ NMR (202 MHz, $CDCl_3$, 294K): δ 118.9 (s, 1P). Anal. Calcd for $C_{28}H_{21}ClIrN_2O_3P$: C, 48.59; N, 4.05; H, 3.06. Found: C, 48.27; N, 4.47; H, 3.32.

Selected crystal data of ***1a***: $C_{28}H_{21}ClIrN_2O_3P$; M = 692.09; monoclinic; space group = $P2_1/c$; a = 14.0496(7) Å, b = 9.9966(5) Å, c = 18.0855(9) Å, β = 107.663(1)°, V = 2420.3(2) Å^3; Z = 4; ρ_{calcd} = 1.899 Mg m^{-3}; $F(000)$ = 1344; crystal size = 0.22 × 0.13 × 0.08 mm^3; λ(Mo Kα) = 0.710 73 Å; T = 150(2) K; μ = 5.728 mm^{-1}; 18 216 reflections collected, 5541 independent reflections (R_{int} = 0.0393), GOF = 1.077, final R_1 [$I > 2\sigma(I)$] = 0.0251 and wR_2 (all data) = 0.0624.

Synthesis of 2a. This complex was synthesized from dbbpy using the procedures reported for **1a** and then purified by silica gel column chromatography using a 1:2 mixture of hexane and ethyl acetate. The green crystals of [Ir(dbbpy)(tpit)Cl] (**2a**) were obtained by the slow diffusion of hexane into a CH_2Cl_2 solution at room temperature (73 mg, 0.09 mmol, 46%).

Spectral Data of ***2a***. MS (FAB, ^{35}Cl, ^{193}Ir): m/z 769 $(M - Cl)^+$. ^1H NMR (500 MHz, $CDCl_3$, 294 K): δ 8.18 (d, J = 7.2 Hz, 2H), 7.86 (d, J = 5.6 Hz, 2H), 7.73 (d, J = 1.6 Hz, 2H), 7.22 (dd, J = 8.0 and 2.0 Hz, 2H), 6.96−6.95 (m, 4H), 6.93−6.85 (m, 2H), 6.75 (t, J = 6.8 Hz, 1H), 6.68 (t, J = 7.2 Hz, 2H), 6.48 (d, J = 8.0 Hz, 2H), 1.35 (s, 18H). $^{31}P\{^1H\}$ NMR (202 MHz, $CDCl_3$, 294 K): δ 119.1 (s, 1P). Anal. Calcd for $C_{36}H_{37}ClIrN_2O_3P$: C, 53.76; N, 3.48; H, 4.64. Found: C, 53.73; N, 3.81; H, 4.48.

Synthesis of 2b. **2a** (50 mg, 0.06 mmol) and KSCN (60 mg, 0.6 mmol) were combined in *N*,*N*-dimethylformamide (DMF; 15 mL), and the mixture was refluxed for 32 h. After cooling to room temperature, the solvent was removed, and the residue was purified by silica gel column chromatography, eluting with a 1:1 mixture of hexane and ethyl acetate. The green crystals of [Ir(dbbpy)(tpit)NCS] (**2b**) were obtained by the slow diffusion of hexane into a CH_2Cl_2 solution at room temperature (42 mg, 0.06 mmol, 82%).

Spectral Data of ***2b***. MS (FAB, ^{193}Ir): m/z 828 $(M + 1)^+$. ^1H NMR (500 MHz, $CDCl_3$, 294 K): δ 7.80 (d, J = 6.0 Hz, 2H), 7.78 (d, J = 0.8 Hz, 2H), 7.73 (d, J = 1.2 Hz, 2H), 7.26 (dd, J = 6.0 and 1.6 Hz, 2H), 6.99−6.94 (m, 4H), 6.91−6.87 (m, 2H), 6.75 (t, J = 7.6 Hz, 1H), 6.67 (t, J = 8.0 Hz, 2H), 6.43 (d, J = 8.4 Hz, 2H), 1.38 (s, 18H). $^{31}P\{^1H\}$ NMR (202 MHz, $CDCl_3$, 294 K): δ 121.8 (s, 1P). Anal. Calcd for $C_{37}H_{37}IrN_3O_3PS$: C, 53.74; N, 5.08; H, 4.51. Found: C, 53.43; N, 5.06; H, 4.78.

Selected crystal data of ***2b***: $C_{37}H_{37}IrN_3O_3PS$; M = 826.93; orthorhombic; space group = *Pbca*; a = 17.9687(8) Å, b = 17.0664(8) Å, c = 21.9546(10) Å, V = 6732.6(5) Å^3; Z = 8; ρ_{calcd} = 1.632 Mg m^{-3}; $F(000)$ = 3296; crystal size = 0.25 × 0.20 × 0.15 mm^3; λ(Mo Kα) = 0.710 73 Å; T = 150(2) K; μ = 4.117 mm^{-1}; 49 982 reflections collected, 7728 independent reflections (R_{int} = 0.0756), GOF = 1.060, final R_1 [$I > 2\sigma(I)$] = 0.0344 and wR_2 (all data) = 0.0666.

Synthesis of 2c. *Method 1.* Complex **2a** (50 mg, 0.06 mmol) and AgOTf (24 mg, 0.09 mmol) were combined in toluene (25 mL), and the mixture was stirred at room temperature for 12 h. After the addition of 3,5-bis(triflouromethyl)-1*H*-pyrazole (bfpzH; 63 mg, 0.31 mmol) and sodium acetate (25 mg, 0.31 mmol), the mixture was stirred at room temperature for another 12 h. Finally, the solvent was removed, and the residue was purified by silica gel column chromatography, eluting with a 2:1 mixture of hexane and ethyl acetate. The green crystals were obtained as [Ir(dbbpy)(tpit)(bfpz)] (**2c**) by the slow diffusion of hexane into a CH_2Cl_2 solution at room temperature (25 mg, 0.03 mmol, 41%).

dx.doi.org/10.1021/ic2003723 |*Inorg. Chem.* 2011, 50, 5075–5084

Method 2. A mixture of **2a** (50 mg, 0.06 mmol), bfpzH (63 mg, 0.31 mmol), and potassium acetate (30 mg, 0.31 mmol) were combined in decalin (15 mL), and the mixture was heated at 180 °C for 24 h. After cooling to room temperature, the solvent was removed, and the residue was purified by silica gel column chromatography, eluting with a 1:2 mixture of hexane and ethyl acetate. Recrystallization from hexane gave the green crystals as **2c** (27 mg, 0.03 mmol, 45%).

Spectral Data of ***2c***. MS (FAB, ^{193}Ir): m/z 973 $(M + 1)^+$. ^{1}H NMR (500 MHz, acetone-d_6, 294 K): δ 8.19 (d, J = 6.0 Hz, 2H), 8.09 (d, J = 1.5 Hz, 2H), 7.54 (dd, J = 6.0 and 1.5 Hz, 2H), 7.51 (d, J = 7.5 Hz, 2H), 6.94−6.83 (m, 7H), 6.73−6.70 (m, 2H), 6.52 (s, 1H), 6.47 (d, J = 8.5 Hz, 2H), 1.37 (s, 18H). ^{31}P{^{1}H} NMR (202 MHz, acetone-d_6, 294 K): δ 119.8 (s, 1P). ^{19}F{^{1}H} NMR (470 MHz, acetone-d_6, 294 K): δ −56.14 (s, 3F), −61.84 (s, 3F). Anal. Calcd for $C_{41}H_{38}F_6IrN_4O_3P$: C, 50.67; N, 5.76; H, 3.94. Found: C, 50.33; N, 5.26; H, 3.65.

Synthesis of 3a. This complex was synthesized from bq using a procedure similar to that reported for **1a** and then purified by silica gel column chromatography using a 3:1 mixture of CH_2Cl_2 and ethyl acetate. The red crystalline solids of [Ir(bq)(tpit)Cl] (**3a**) were obtained by the slow diffusion of hexane into a CH_2Cl_2 solution at room temperature (56 mg, 0.08 mmol, 42%).

Spectral Data of ***3a***. MS (FAB, ^{35}Cl, ^{193}Ir): m/z 757 $(M - Cl)^+$. ^{1}H NMR (500 MHz, $CDCl_3$, 294 K): δ 8.49 (d, J = 9.5 Hz, 2H), 8.25 (d, J = 5.0 Hz, 1H), 8.23 (d, J = 9.5 Hz, 3H), 7.97 (d, J = 8.5 Hz, 2H), 7.70 (d, J = 8.0 Hz, 2H), 7.46 (t, J = 7.5 Hz, 2H), 7.27 (t, J = 8.0 Hz, 2H), 6.84−6.83 (m, 4H), 6.76−6.74 (m, 2H), 6.71 (t, J = 7.5 Hz, 1H), 6.32 (t, J = 8.0 Hz, 2H), 6.51 (d, J = 8.0 Hz, 2H). ^{31}P{^{1}H} NMR (202 MHz, $CDCl_3$, 294 K): δ 113.4 (s, 1P). Anal. Calcd for $C_{36}H_{25}ClIrN_2O_3P$: C, 54.58; N, 3.54; H, 3.18. Found: C, 54.36; N, 3.98; H, 3.49.

Single-Crystal X-ray Diffraction Studies. Single-crystal X-ray diffraction data were measured with a Bruker SMART Apex CCD diffractometer using Mo Kα radiation (λ = 0.710 73 Å). The data collection was executed using the *SMART* program. Cell refinement and data reduction were performed with the *SAINT* program. The structure was determined using the *SHELXTL/PC* program and refined using full-matrix least squares.

Photophysical Investigation. Steady-state absorption, emission, and phosphorescence lifetime measurements in solution and the solid state were described in our previous reports.[12] To determine the photoluminescence quantum yield in solution, the samples were degassed by three freeze−pump−thaw cycles. 4-(Dicyanomethylene)-2-methyl-6-[*p*-(dimethylamino)styryl]-4*H*-pyran (DCM; λ_{max} = 615 nm, exciton) in methanol, with a quantum yield of ∼0.44, served as the standard for measurement of the quantum yield. Lifetime studies were performed with an Edinburgh FL 900 photon-counting system using a hydrogen lamp as the excitation source. Data were analyzed using a nonlinear least-squares procedure in combination with an iterative convolution method. The emission decays were fitted by the sum of exponential functions with a temporal resolution of ∼300 ps after deconvolution of the instrument response function.

Computational Methodology. Calculations on the electronic singlet and triplet states of all titled complexes were carried out using DFT with the B3LYP hybrid functional.[13] Restricted and unrestricted formalisms were adopted in the singlet and triplet geometry optimizations, respectively. A "double-ζ" quality basis set consisting of Hay and Wadt's effective core potentials (ECPs; LANL2DZ)[14] was employed for the Ir^{III} metal atom, and a 6-31G* basis set,[15] for the rest of the atoms. The relativistic ECP replaced the inner-core electrons of the Ir^{III} metal atom, leaving only the outer-core valence electrons ($5s^25p^65d^6$) to be concerned with. Time-dependent DFT (TDDFT) calculations using the B3LYP functional were then performed based on the optimized structures at ground states.[16] Moreover, considering the solvation effect, the calculations were then combined with an integral equation formalism polarizable continuum model (IEF-PCM; in dichloromethane), implemented in *Gaussian 03*.[17] Typically, 10 lower triplet and singlet roots of the nonhermitian eigenvalue equations were obtained to determine the vertical excitation energies. Oscillator strengths were then deduced from the dipole transition matrix elements (for singlet states only). All calculations were carried out using *Gaussian 03*.[18]

RESULTS AND DISCUSSION

Synthetic Strategy. Synthesis of the required iridium(III) metal complexes was accomplished using the $[IrCl_3(tht)_3]$ metal reagent, which is highly soluble in nonpolar, higher-boiling hydrocarbon solvents such as decalin. Moreover, the experiments were performed using procedures reported for the synthesis of relevant iridium(III) complexes employing benzyldiphenylphosphine cyclometalates.[19] Thus, upon the addition of an equimolar amount of $tpitH_2$ and diimine such as bpy, dbbpy, and bq, we were able to obtain a series of novel diimine complexes, **1a**, **2a**, and **3a**, in high yields. Scheme 2 depicts the structural drawings of these iridium(III) complexes. It is believed that the added diimine and phosphite would easily replace all three tht ligands and then form certain unknown intermediates at the beginning of the reaction. Moreover, the phosphite coordination would bring two of its phenyl substituents near the central Ir^{III} atom and then facilitate subsequent double cyclometalation with assistance from sodium acetate added to the mixture. Further cyclometalation of the last phenyl group is considered to be infeasible because of the geometrical constraint imposed by the phosphite-chelating conformation.

In addition to the tripodal phosphite, it is interesting to note that all of the complexes **1a**−**3a** possess a terminal chloride ligand at the sixth coordination site, a result that is in sharp contrast to the previous reaction pattern involving phosphine, for which the removal of all chloride in the presence of acetate has been documented.[20] However, anion metathesis was successfully achieved using a higher-boiling, polar solvent under extended heating or upon the addition of a silver reagent as the chloride scavenger. Accordingly, complex **2a** reacts with KNCS and bis(trifluoromethyl)-1*H*-pyrazole to form thiocyanate and

Scheme 2. Structural Drawings of the Iridium(III) Diiminephosphite Complexes

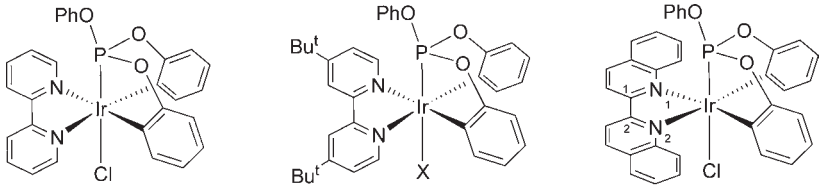

dx.doi.org/10.1021/ic2003723 |*Inorg. Chem.* 2011, 50, 5075–5084

pyrazolate derivatives **2b** and **2c** in moderate yields, respectively. Moreover, the thiocyanate-substituted **2b** appears to be reasonably stable in solution, but the pyrazolate complex **2c** can be partially converted back to its parent complex **2a** in a chlorinated solvent such as $CHCl_3$ at room temperature within approximately 24 h.

Structural Determination. Single crystals suitable for X-ray structural analysis were grown by the slow diffusion of hexane into the CH_2Cl_2 solution at room temperature. The X-ray structural determinations were conducted on complexes **1a** and **2b** to confirm their coordination features. Figures 1 and 2 show their ORTEP diagrams, together with the selected metric parameters that are listed in the caption. As one can clearly perceive, the Ir^{III} metal center in both complexes formed a distorted octahedral coordination arrangement. The phosphite tripod occupies the *facial* dispositions, among which the P atom is tilted toward both phenyl cyclometalates because of an internal constraint setting up by the oxygen linkers. The bpy chelate and the dual phenyl cyclometalates adopt the square-planar geometry. This planar arrangement then allows the remaining phenyl pendent of phosphite to stack favorably with bpy. The associated intramolecular $\pi\pi$-stacking interaction is confirmed by the short phenyl-to-pyridine hexagonal center-to-center contact of 3.573 Å, as observed in **1a**. On the other hand, for complex **2b**, because of the presence of *tert*-butyl substituents on the bipyridine, the relevant center-to-center contact now increased to 3.651 Å, showing a reduction of the $\pi\pi$-stacking interaction attributed to the increased steric demand. Finally, the ambidentate thiocyanate ligand of complex **2b** is linked to the Ir^{III} metal atom via its N atom and retained a linear arrangement; such a bonding mode is identical with that observed in many structurally characterized ruthenium(II) and iridium(III) complexes.[21]

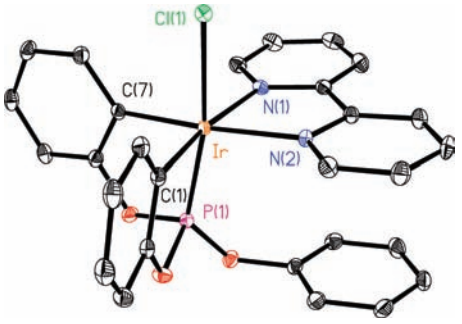

Figure 1. ORTEP diagram of **1a** with ellipsoids shown at the 30% probability level. Selected bond distances (Å): Ir−P(1) = 2.1441(10), Ir−Cl(1) = 2.4455(9), Ir−C(7) = 2.051(4), Ir−C(1) = 2.054(4), Ir−N(1) = 2.134(3), and Ir−N(2) = 2.145(3).

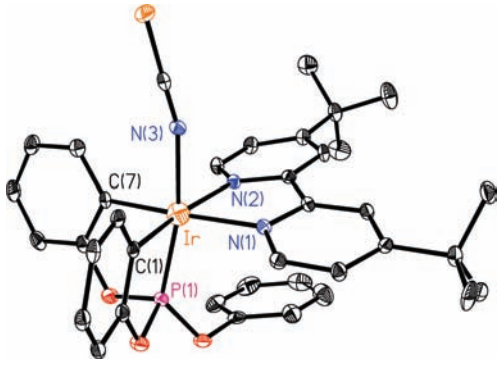

Figure 2. ORTEP diagram of **2b** with ellipsoids shown at the 30% probability level. Selected bond distances (Å): Ir−P(1) = 2.1486(10), Ir−N(3) = 2.086(3), Ir−C(7) = 2.048(4), Ir−C(1) = 2.054(4), Ir−N(1) = 2.123(3), and Ir−N(2) = 2.125(3).

Electrochemistry. The electrochemical behavior of these iridium(III) metal complexes was investigated by CV using ferrocene as the internal standard. The respective redox data are listed in Table 1. During the anodic scan in CH_2Cl_2, all iridium(III) metal complexes exhibited an irreversible oxidation peak occurring in the region 0.89−1.01 V, which is assigned as the metal-centered oxidation process. As a result, these potentials are less affected by variation of diimine chelate. This viewpoint is confirmed by the fact that only smaller variations from 0.89 to 0.95 V are observed for the set of chloride complexes **1a**, **2a**, and **3a**. On the other hand, variation of the anionic ligand from chloride (**2a**) and bfpz (**2c**) to thiocyanate (**2b**) has produced a notable change from 0.89 and 0.90 to 1.01 V. This was attributed to the much reduced electron-donating capability of thiocyanate in **2b**.

Upon switching to the cathodic sweep in tetrahydrofuran (THF), a single quasi-reversible peak potential ranging from −2.33 to −2.78 V was also detected. As revealed by previous studies, the reduction occurred mainly at the π^* orbital of the diimine chelate. Accordingly, the lowest reduction peak potential of −2.33 V is detected in complex **3a**, for which the extended π conjugation of bq would afford the lowest potential for the incoming electron. In contrast, all of the complexes **2a**−**2c** would afford many negative reduction potentials because of the presence of two electron-donating *tert*-butyl groups on bipyridine versus a simple bipyridine or biquinoline chelate.

Photophysical Properties. The photophysical properties of these iridium(III) complexes can be systematically tuned via modification of the diimine chromophores and/or the ancillary ligands. Figure 3 displays the absorption and emission spectra of all titled complexes, **1a**, **2a**−**2c**, and **3a**, recorded in degassed CH_2Cl_2 at room temperature, while pertinent numerical data are

Table 1. Electrochemical and Photophysical Data of Iridium(III) Complexes at Room Temperature

	UV/vis data, nm ($\varepsilon \times 10^{-3}$, M^{-1} cm^{-1})	PL λ_{max} (nm)	QY [a] (%)	τ_{obs} [a] (μs)	k_r (s^{-1})	k_{nr} (s^{-1})	E_{ox} [b]	E_{red} [b]
1a	265sh (15.4), 302sh (14.6), 308 (15.7), 432 (0.67)	574	0.48	0.84	5.77×10^5	6.15×10^5	0.92	−2.53
2a	267sh (15.1), 298sh (13.3), 305 (13.9), 415 (0.64)	557 [517]	0.86	1.36 [1.39]	6.32×10^5	1.0×10^5	0.89	−2.66
2b	275sh (15.5), 297 (14.9), 308 (14.5), 410 (0.70)	552 [500]	0.59	1.50 [1.96]	3.91×10^5	2.76×10^5	1.01	−2.57
2c	283sh (11.8), 300 (14.6), 399 (0.91)	562	0.29	1.32	2.2×10^5	5.4×10^5	0.90	−2.78
3a	274 (48.1), 353sh (17.9), 370 (23.0), 487 (1.47)	646	0.11	0.33	3.39×10^5	2.74×10^6	0.95	−2.33

[a] Samples were degassed and recorded in CH_2Cl_2 at room temperature with ε in M^{-1} cm^{-1}, while photophysical data recorded in the solid state are depicted in square brackets. [b] All electrochemical potentials were measured in a 0.1 M $TBAPF_6/CH_2Cl_2$ and THF solution for oxidation and reduction reactions and are reported in volts using Fc/Fc^+ as the reference. Both E_{ox} and E_{red} are referred to the irreversible peak potential. The glassy carbon and gold−mercury alloy were selected as the working electrodes of oxidation and reduction processes, respectively.

dx.doi.org/10.1021/ic2003723 |*Inorg. Chem.* 2011, 50, 5075–5084

summarized in Table 1. In general, all of the complexes **1a** and **2a**−**2c** exhibit allowed absorption bands in the UV region of <300 nm (and <400 nm for **3a**), for which ε values at the peak maxima are measured to be >1.5 × 10^4 M^{-1} cm^{-1} and can thus be attributed to a ligand-centered $\pi\pi^*$ transition. The broad band at longer wavelength of up to 400 nm for complexes **1a** and **2a**−**2c** (500 nm for **3a**), as revealed by their relatively lower extinction coefficients (<3 × 10^3 M^{-1} cm^{-1}), is assigned to the tail of the $\pi\pi^*$ transition overlapping with the MLCT transition in the singlet manifold. Furthermore, complex **3a** showed a significant gain in absorptivity, and all peaks are very red-shifted compared to those of other complexes, manifesting the influence of extended π conjugation on the quinoline (cf. pyridine) moiety. As for the emission spectra, the significant variation of the intensity between aerated and degassed solutions, i.e., the great influence of O_2 quenching, together with the long radiative lifetime (approximately microseconds; see Table 1), indicates that the emission originates from the triplet manifold, i.e., the phosphorescence. All of the titled complexes exhibit broad, structureless emission within the range of 450−750 nm for **1a** and **2a**−**2c** and 550−850 nm for **3a**. It is noteworthy that the spectral profiles of both absorption and emission for **1a**, **2a**−**2c**, and **3a** are independent of the concentrations prepared, eliminating the possible $\pi\pi$ interaction of the titled complexes in solution in both ground and excited states.

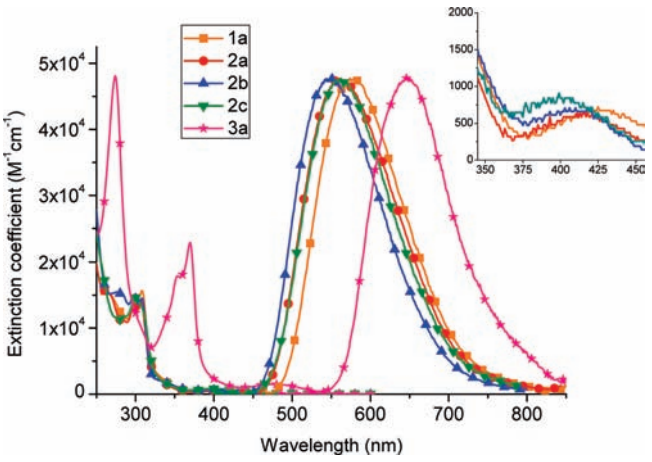

Figure 3. Absorption and luminescence spectra of **1a**, **2a**−**2c**, and **3a** in a degassed CH_2Cl_2 solution at room temperature. The inset shows the absorption spectra of complexes **1a** and **2a**−**2c** in the region of 350−450 nm.

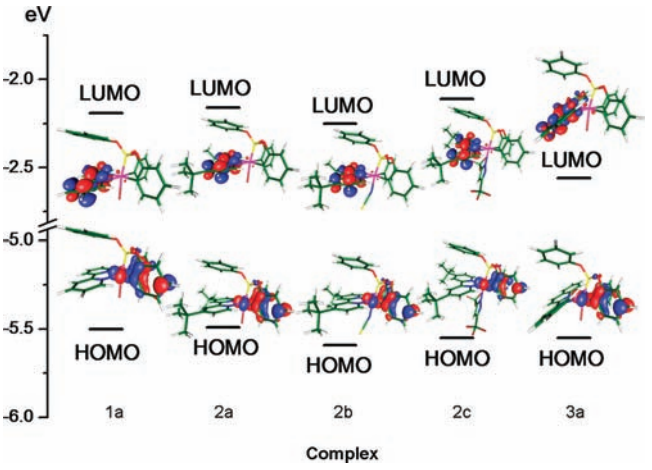

Figure 4. Frontier orbitals involved in the lowest-lying electronic transitions for **1a**, **2a**−**2c**, and **3a**. Calculations were done with incorporation of the PCM model in CH_2Cl_2.

Apparently, the extension of π conjugation on biquinoline in **3a** substantially decreases the lowest unoccupied molecular orbital (LUMO; π^*) energy (cf. the bipyridine moiety) and, hence, reduces the emission gap. In addition, **3a** gives the lowest quantum yield among all of the studied complexes; cf. Φ_{1a} = 0.48, Φ_{2a} = 0.86, Φ_{2b} = 0.59, Φ_{2c} = 0.29, and Φ_{3a} = 0.11. For **3a**, the reduction of the $\pi\pi^*$ gap should enlarge the energetic difference between the emitting ^{3}MLCT/$\pi\pi^*$ state and the higher-lying ^{3}MC dd state; the latter commonly induces a nonradiative pathway due to weakening of the metal−ligand bond. Accordingly, suppression of the ^{3}MC dd population, in theory, should lead to a higher quantum yield in **3a**. While the dicyclometalated phosphite and chloride ancillaries are identical among complexes **1a**, **2a**, and **3a**, the apparent opposite result, i.e., the lowest Φ_p for **3a** among all titled complexes, is thus intriguing. The main quenching process for a red emitter such as **3a** with emission maximized at 650 nm may be attributed to high-frequency vibrational deactivation, i.e., the operation of the energy gap law.[22] In addition, other deactivation pathways associated with substantial geometric distortion of the diimine ligand occurring between the ground and emitting states cannot be eliminated. Support of this viewpoint is provided in the section on the theoretical approach (vide infra).

Table 2. Calculated Wavelength (λ), Oscillator Strength (f), and Orbital Transition Analyses of 1a, 2a−2c, and 3a Incorporated with the PCM Model of Dichloromethane[a]

	states	λ_{cal}	f	assignments	MLCT (%)
1a	T_1	477	0	HOMO → LUMO (98%)	33.76
	S_1	469.8	0.0053	HOMO → LUMO (98%)	33.76
2a	T_1	467.8	0	HOMO → LUMO (98%)	33.82
	S_1	465.3	0.0061	HOMO → LUMO (98%)	33.82
2b	T_1	464 [645.6]	0	HOMO → LUMO (98%) [HOMO → LUMO (100%)]	32.35 [4.62]
	S_1	460.6 [643.1]	0.0074 [0.0001]	HOMO → LUMO (99%) [HOMO → LUMO (100%)]	32.68 [4.62]
2c	T_1	453.3	0	HOMO → LUMO (95%)	33.62
	S_1	446.9	0.0067	HOMO → LUMO (98%)	34.68
3a	T_1	545.3	0	HOMO → LUMO (94%)	32.08
	S_1	521.9	0.035	HOMO → LUMO (97%)	33.11

[a] Data shown in brackets are calculated in the gas phase.

dx.doi.org/10.1021/ic2003723 |*Inorg. Chem.* 2011, 50, 5075–5084

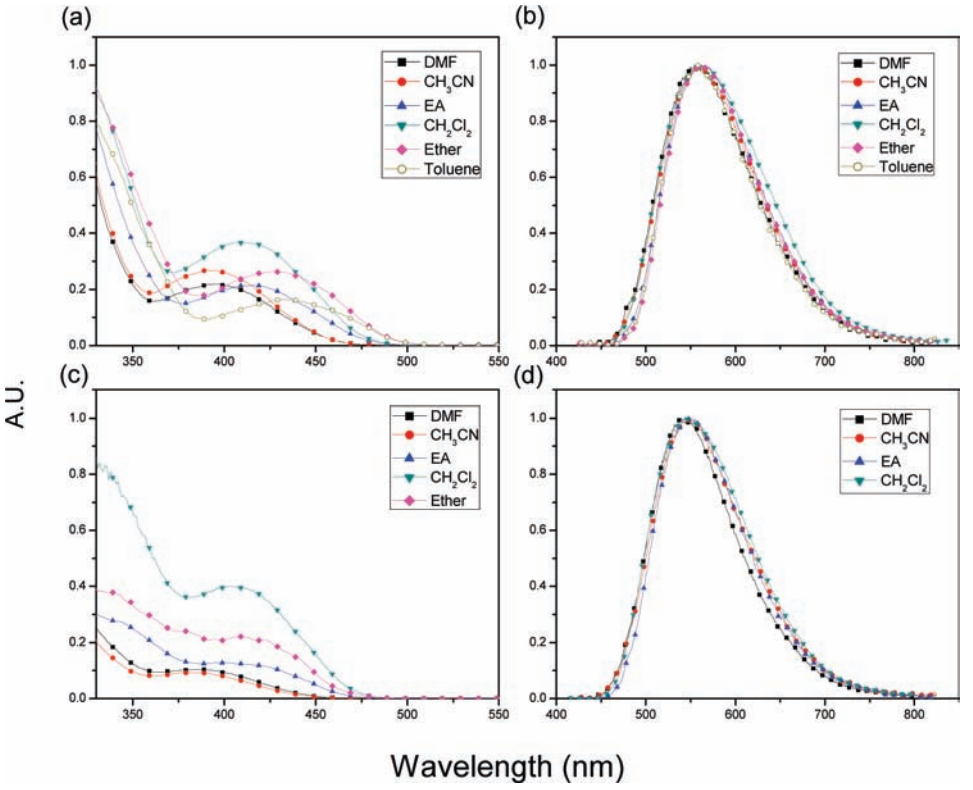

Figure 5. Absorption and luminescence spectra of **2a** (a and b) and **2b** (c and d) resolved in different degassed solvents at room temperature.

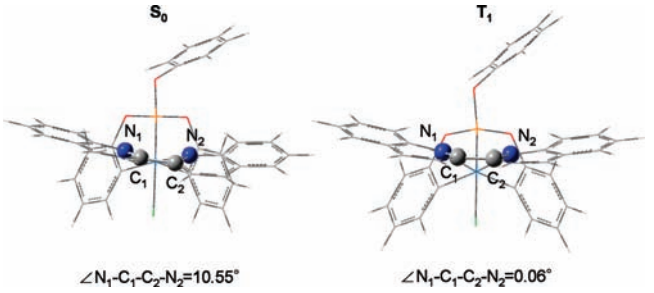

Figure 6. Optimized structures at the ground state (S_0) and the lowest triplet state (T_1) for **3a**, respectively.

In order to gain in-depth information about the absorptive and emissive properties, TDDFT was then performed via use of the functional B3LYP and the 6-31G(d)/LANL2DZ basis set. Also, the PCM model in CH_2Cl_2 is incorporated to take the solvation effect into account (see the Experimental Section for details). Figure 4 depicts the selected frontier orbitals involved in lower-lying transitions of the titled complexes. The calculated energy gaps and corresponding assignments of each transition are listed in Table 2. The calculated $S_0 \rightarrow S_1$ transition (in terms of wavelength) of all studied complexes (**1a**, 469.8 nm; **2a**, 465.3 nm; **2b**, 460.6 nm; **2c**, 446.9 nm; **3a**, 521.9 nm) are close to the observed onsets of the absorption spectra depicted in Figure 3. Moreover, the calculated energy gaps of the T_1 states (**1a**, 477 nm; **2a**, 467.8 nm; **2b**, 464 nm; **2c**, 453.3 nm; **3a**, 545.3 nm) are qualitatively in agreement with the onsets (i.e., blue edge) of their emission spectra. This result indicates that the TDDFT calculation works well in predicting the lowest Franck−Condon excited state for both absorption and emission based on the S_0-optimized geometries of all complexes.

As for the transition characteristics, frontier orbital analyses indicate that the lowest singlet excited states (S_1) for all complexes are primarily attributed to the HOMO → LUMO transition (cf. Table 2). As depicted in Figure 4, the HOMO of all titled complexes is mainly localized at the central Ir^{III} metal atom and phenyl cyclometalates of phosphite, while the LUMO is located at the diimine moiety, implying that the lowest-lying absorption transition mainly involves the MLCT transition and interligand (phenyl → diimine) charge transfer (LLCT). Because of the large separation in terms of distance and orientation between chromophores, the latter may cause a significant change of the dipole moment between ground and excited states. This is clearly demonstrated by the strong solvent-polarity-dependent absorption spectra for, e.g., **2a** and **2b**, shown in Figure 5 (vide infra). Also, as shown in Table 2, the calculated % MLCT for both S_1 and T_1 states is >30% for all titled complexes, resulting in a strong spin−orbit coupling, i.e., a great mixing between the S_1 and T_1 states, due to the direct involvement of the heavy Ir^{III} metal atom. Support of this viewpoint is also given by the small energy gap between S_1 and T_1 (see Table 2) as well as the close onset between S_0−S_1 absorption and phosphorescence (see Figure 3). As for the chemical substitution effect, compared with complexes **1a** and **2a**−**2c** exhibiting more blue-shifted emission profiles, this can be rationalized by an increase of the LUMO energy via the *tert*-butyl substituents imposed on the diimine moiety.

Careful examination of the optimized structures of **3a** reveals an intriguing geometry in the lower-lying excited states. While the optimized structure of **3a** in the ground state (S_0) shows a twisted, nonplanar configuration along the biquinolinyl moiety, the relaxed geometry in the T_1 state reveals a planar structure.

dx.doi.org/10.1021/ic2003723 |*Inorg. Chem.* 2011, 50, 5075–5084

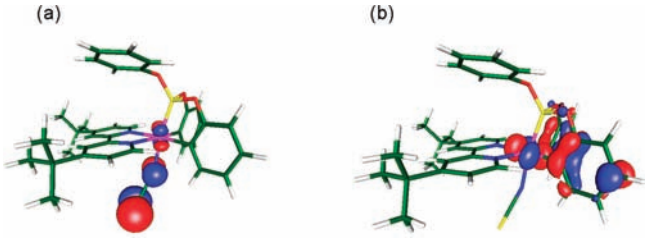

Figure 7. HOMO of **2b** calculated (a) in the gas phase and (b) in CH_2Cl_2 incorporated with the PCM model.

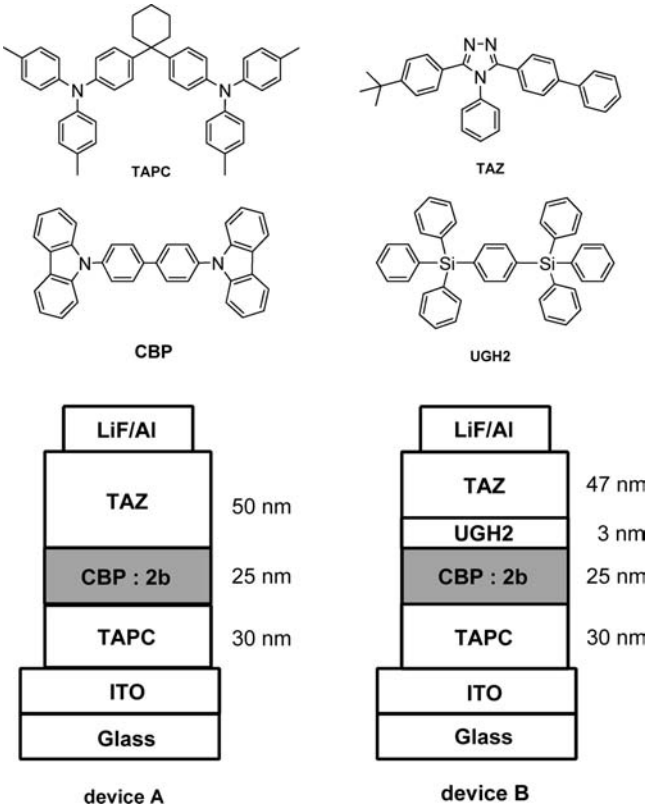

Figure 8. Structural drawing of the materials and schematic structures of green-emitting OLEDs.

This difference is evidenced by the dihedral angle $\angle N_1-C_1-C_2-N_2$ of 10.55° and 0.06° at the S_0 and T_1 states, respectively (see Scheme 2 and Figure 6). Thus, despite the seemingly more π conjugation in **3a**, the substantial structural differences between the optimized S_0 and T_1 states may thus execute the $T_1 \rightarrow S_0$ radiationless transition; that is, the high-density, low-frequency vibrations associated with the changes of geometry in S_0 may couple with the T_1 lower-lying vibronic states to channel into the deactivation pathway.[22c]

It should be noted that the above computational approach incorporates the PCM model to take the solvation effect (e.g., in CH_2Cl_2) into consideration. Amid the calculation, we noticed that the solvation effect plays a crucial role in influencing the electronic distribution, especially for **2b** possessing a thiocyanate ancillary. In the gas phase, the electron densities of the highest occupied molecular orbital (HOMO) calculated for **2b** are mainly distributed on the thiocyanate group (see Figure 7). This result is in sharp contrast to that obtained in CH_2Cl_2, in which the electron density of the HOMO is then redistributed and located at the central Ir^{III} metal atom and phenyl cyclometalates of the phosphite tripod (see Figures 4 and 7). Compared with the experimental data, the computation incorporating the solvation model seems to give more reliable results. First of all, in the gas phase, the calculated S_1 state for **2b** is located at 643 nm, which is very red-shifted with respect to the onset of the experimental lowest-lying absorption (~450−470 nm). Alternatively, calculation involving CH_2Cl_2 solvation predicts a close S_1 energy of 460 nm. Note that the calculated blue shift of the $S_0 \rightarrow S_1$ absorption upon an increase in the polarity (gas → CH_2Cl_2) is consistent with the experimental observation (see Figure 7). Second, in the gas phase, a small proportion of MLCT in both S_1 (4.62%) and T_1 states (4.62%) (see Table 2) is estimated. The dominant $\pi\pi^*$ character for the T_1 state predicts a less allowed T_1-S_0 phosphorescence and, hence, a much smaller radiative decay rate constant. This is apparently contradictory to the experimentally resolved k_r value of as large as 3.91×10^5 s^{-1}. Alternatively, the >33% MLCT contribution for the T_1 state calculated in CH_2Cl_2 (see Table 2) well-rationalizes the experimental data.

Finally, as shown in Figure 5, the negative absorption solvatochromism for **2a** and **2b** can be rationalized in terms of a reduced excited-state dipole moment upon MLCT/LLCT excitation.[4] We then calculate the dipole moment of, e.g., **2a** in both S_0 and S_1 states. The dipole moment of the excited state (S_1) is calculated via the Hellmann−Feynman theory, which can be estimated by the analytical derivative of the energy of the excited state with respect to an applied electric field. All details were described in our previous reports.[23] As a result, the calculated dipole moment of 15.45 D in S_0 is larger than that (3.18 D) in S_1. In addition, the dipole orientation of the S_0 state is 52.7° with respect to that of the S_1 state. Thus, a substantial change of the dipole moment of 13.75 D between S_0 and S_1 is deduced, supporting the absorption solvatochromism. Despite the solvent-polarity-dependent absorption, however, the emission profiles of **2a** and **2b** reveal nearly solvent-polarity independence (see Figure 5). We attribute the results to compensation of an offset between absorption and emission. A more blue shift in the absorption results in a greater difference in the dipole moment between the ground and excited states. Thus, the emission is subject to larger solvent relaxation/stabilization, giving virtually nearly solvent-polarity-independent emission spectra.

OLED Device Fabrication. Complex **2b** is next selected as the dopant for the fabrication of phosphorescent OLEDs because of its higher stability and photoluminescence quantum efficiency. The devices consist of a simplified three-layer architecture of indium−tin oxide (ITO)/TAPC (30 nm)/CBP doped with 8 wt % **2b** (25 nm)/electron-transport layer (ETL; 50 nm)/LiF (0.8 nm)/Al (150 nm), for which the configurations and structural drawings of essential materials are shown in Figure 8. Several different types of electron-transport materials were utilized for investigating the effect of the carrier balance, including 1,3,5-tris[(3-pyridyl)phen-3-yl]benzene (TmPyPB), 2,2′,2″-(1,3,5-benzinetriyl)tris(1-phenyl-1*H*-benzimidazole), 2,9-dimethyl-4,7-diphenyl-1,10-phenanthroline, bis(2-methyl-8-quinolinolate)-4-(phenylphenolato)aluminum, and 3-(4-biphenylyl)-4-phenyl-5-(*tert*-butylphenyl)-1,2,4-triazole (TAZ). The electron mobility of these materials ranges from ~10^{-6} (TAZ) to ~10^{-3} cm^2 V^{-1} s^{-1} (TmPyPB).[24] However, all devices gave very similar maximum external quantum efficiencies of 11−13%, showing that the electron mobility is not the dominant factor for

dx.doi.org/10.1021/ic2003723 |*Inorg. Chem.* 2011, 50, 5075–5084

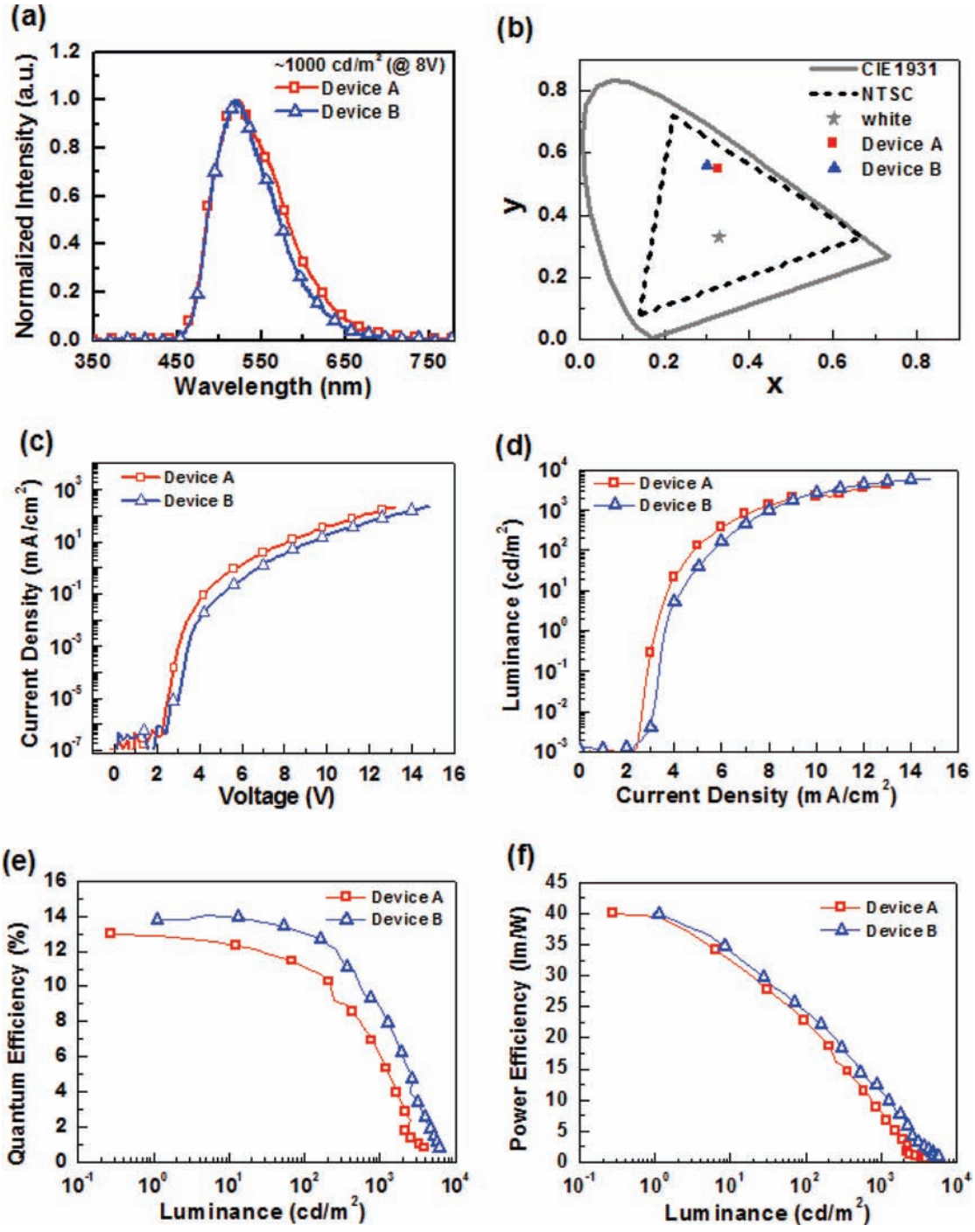

Figure 9. (a) EL spectra, (b) CIE coordinates, (c) current density−voltage ($I-V$) characteristics, (d) luminescence vs voltage, (e) external quantum efficiency vs luminance, and (f) power efficiencies vs luminance for devices A and B.

device performances. Upon careful inspection of the carrier balance in this system, one can see that TAPC possesses a higher hole mobility ($\sim 10^{-2}$ cm^2 V^{-1} s^{-1}) than that of all tested electron-transport materials.[25] In addition, the host material, CBP, possesses a bipolar property, implying that the dopant played a key role in manipulating the carrier balance in the emitting layer.[26] Hence, one could expect that dopant **2b** functions as effective hole traps in the emitting layer, thereby hindering excessive hole transport.[27] Thus, the lower hole mobility of CBP doped with **2b** would be in favor of balancing carrier transport in the emitting layer, after considering the electron mobility of all electron-transport materials.

One optimized device was next fabricated using TAZ as the ETL; cf. device A. It exhibited peak electroluminescent (EL) efficiencies of 13.0% photon/electron, 40.3 cd A^{-1}, and 40 lm W^{-1} for the forward directions. Under a more practical brightness of 100 cd m^{-2}, the forward viewing efficiencies remained high, at around 10.9%, 33.9 cd A^{-1}, and 21.3 lm W^{-1}. However, the predominantly green emission of **2b** was accompanied with a notable near-UV emission at higher current densities, which is

dx.doi.org/10.1021/ic2003723 |*Inorg. Chem.* 2011, 50, 5075–5084

Table 3. EL Characteristics of Green-Emitting OLEDs Using Complex 2b with Different ETL

	η_{ext} (%)		η_l (cd A^{-1})		η_p (lm W^{-1})		V_{on} (V)	max. B.	CIE coordinates	
	max.	10^2 nit	max.	10^2 nit	max.	10^2 nit	1 nit	nit (V)	10^2 nit	10^3 nit
Device A (TAZ)	13.0	10.9	40.3	33.9	40.0	21.3	3.1	4124 (13.2 V)	(0.302, 0.561)	(0.329, 0.545)
Device B (UGH2/TAZ)	14.1	12.7	46.6	42.0	39.9	22.0	3.6	6125 (14.8 V)	(0.298, 0.564)	(0.302, 0.557)

Abbreviations: η_{ext} = external quantum efficiency; η_l = luminescence efficiency; η_p = power efficiency; V_{on} = turn-on voltage; max. B = maximum brightness; nit = cd m^{-2}.

attributed to the carrier recombination in the ETL (TAZ is known to exhibit near-UV emission at ~400 nm).[24] To diminish the unwanted emission and to further improve the efficiency, the wide-gap material UGH2, which possesses a rather large triplet energy gap of 3.18 eV, was employed to give optimal carrier/exciton confinement.[28] The modified architecture (i.e., device B) consisted of ITO/TAPC (30 nm)/CBP doped with 8 wt % **2b** (25 nm)/UGH2 (3 nm)/TAZ (47 nm)/LiF (0.8 nm)/Al (150 nm). Figure 9 shows the EL spectra of these two green-emitting devices. Obviously, the near-UV emission generated from TAZ in device A was effectively reduced after employment of a thin layer of UGH2. Such an outcome indicates the successful confinement of carrier recombination or blockage of exciton diffusion into the charge-transport layer.

The current−voltage−luminance (I−V−L) characteristics and other EL performance data are also depicted in Figure 9 and Table 3. The peak external quantum efficiency (η_{ext}), luminance efficiency (η_l), and power efficiency (η_p) of device B were increased to 14.1%, 46.6 cd A^{-1}, and 39.9 lm W^{-1}, respectively. Such high external quantum efficiencies implied a high internal quantum efficiency of nearly 70% in device B (assuming ~20% optical out-coupling efficiency from the devices). Again, these results confirmed the effectiveness of the buffer layer for achieving effective carrier/exciton confinement. Upon an increase in the practical brightness to 100 cd m^{-2}, η_{ext}, η_l, and η_p remained above 12.7%, 42.0 cd A^{-1}, and 22.0 lm W^{-1}, which are consistent with less significant efficiency roll-offs, with Commission Internationale de L'Eclairage (x, y) coordinates ($CIE_{x,y}$) of (0.298, 0.564). In the mean time, the luminance reached its maximum of 6125 cd m^{-2} at a driving voltage of 14.8 V.

CONCLUSION

In summary, the design and synthesis of a series of iridium(III) complexes functionalized with both diimine and tripodal dicyclometalated phosphite present a novel strategy in achieving highly efficient phosphorescence in the range of blue-green to red. This configuration possesses MLCT (~30%)/LLCT (~70%) character in the lowest-lying transition, which induces strong mixing between the singlet and triplet manifolds and the absorption solvatochromism effect. The latter is echoed by the theoretical approach, indicating that the electron distribution among various chromophores is subject to the solvent-polarity perturbation. The computational results of the HOMO of **2b** show a dominant electron population at the thiocyanate site in the gas phase, while it switches to iridium(III) metal and phenyl moieties in a CH_2Cl_2 solution. This brings attention to the thiocyanate-containing transition complexes, especially those of ruthenium(II) dyes suited for solar energy cells, in that the theoretical approach to their photophysical properties may take the solvent effect into serious consideration. As for the practical application, fabrication of the green-emitting OLEDs with dopant **2b** has been successfully made, attaining a peak external quantum efficiency (η_{ext}), a luminance efficiency (η_l), and a power efficiency (η_p) of 14.1%, 46.6 cd A^{-1}, and 39.9 lm W^{-1}, respectively. We thus believe that the new ligand design and corresponding synthetic strategy should add an additional avenue to promote the research field relevant to phosphorescent OLEDs.

ASSOCIATED CONTENT

Supporting Information. X-ray crystallographic data file (CIF) of the studied complexes **1a** and **2b**. This material is available free of charge via the Internet at http://pubs.acs.org.

AUTHOR INFORMATION

Corresponding Author

*E-mail: ychi@mx.nthu.edu.tw (Y.C.), chop@ntu.edu.tw (P.-T.C.), chc@saturn.yzu.edu.tw (C.-H.C.).

ACKNOWLEDGMENT

This work was supported by the National Science Council of Taiwan. We are also grateful to the National Center for High-Performance Computing for computer time and facilities.

REFERENCES

(1) (a) Yoon, T. P.; Ischay, M. A.; Du, J. *Nat. Chem.* **2010**, *2*, 527. (b) Masciocchi, C. N.; Pandolfo, L.; Pucci, D. *Chem.—Eur. J.* **2010**, *16*, 1106. (c) Ward, M. D. *Dalton Trans.* **2010**, *39*, 8551. (d) Hudson, Z. M.; Wang, S. *Acc. Chem. Res.* **2009**, *42*, 1584. (e) Sakai, K.; Ozawa, H. *Coord. Chem. Rev.* **2007**, *251*, 2753. (f) Marin, V.; Holder, E.; Hoogenboom, R.; Schubert, U. S. *Chem. Soc. Rev.* **2007**, *36*, 618. (g) Maury, O.; Le Bozec, H. *Acc. Chem. Res.* **2005**, *38*, 691. (h) Hissler, M.; McGarrah, J. E.; Connick, W. B.; Geiger, D. K.; Cummings, S. D.; Eisenberg, R. *Coord. Chem. Rev.* **2000**, *208*, 115. (i) Stufkens, D. J.; Vlcek, A., Jr. *Coord. Chem. Rev.* **1998**, *177*, 127.

(2) (a) Vlcek, A.; Busby, M. *Coord. Chem. Rev.* **2006**, *250*, 1755. (b) Takeda, H.; Ishitani, O. *Coord. Chem. Rev.* **2010**, *254*, 346.

(3) (a) Chou, P.-T.; Chi, Y. *Eur. J. Inorg. Chem.* **2006**, 3319. (b) Wong, W.-Y. *Dalton Trans.* **2007**, 4495. (c) Chou, P.-T.; Chi, Y. *Chem.—Eur. J.* **2007**, *13*, 380. (d) Chi, Y.; Chou, P.-T. *Chem. Soc. Rev.* **2007**, *36*, 1421. (e) Williams, J. A. G.; Develay, S.; Rochester, D. L.; Murphy, L. *Coord. Chem. Rev.* **2008**, *252*, 2596. (f) You, Y.; Park, S. Y. *Dalton Trans.* **2009**, 1267. (g) Wong, W.-Y.; Ho, C.-L. *J. Mater. Chem.* **2009**, *19*, 4457. (h) Wong, W.-Y.; Ho, C.-L. *Coord. Chem. Rev.* **2009**, *253*, 1709. (i) Ulbricht, C.; Beyer, B.; Friebe, C.; Winter, A.; Schubert, U. S. *Adv. Mater.* **2009**, *21*, 4418. (j) Chi, Y.; Chou, P.-T. *Chem. Soc. Rev.* **2010**, *39*, 638. (k) Chen, Z.-Q.; Bian, Z.-Q.; Huang, C.-H. *Adv. Mater.* **2010**, *22*, 1534. (l) Duan, L.; Hou, L.; Lee, T.-W.; Qiao, J.; Zhang, D.; Dong, G.; Wang, L.; Qiu, Y. *J. Mater. Chem.* **2010**, *20*, 6392.

(4) (a) Lees, A. J. *Chem. Rev.* **1987**, *87*, 711. (b) Manuta, D. M.; Lees, A. J. *Inorg. Chem.* **1986**, *25*, 3212.
(5) (a) Schanze, K. S.; MacQueen, D. B.; Perkins, T. A.; Cabana, L. A. *Coord. Chem. Rev.* **1993**, *122*, 63. (b) Vogler, A.; Kunkely, H. *Coord. Chem. Rev.* **2000**, *200*, 991. (c) Vlcek, A.; Busby, M. *Coord. Chem. Rev.* **2006**, *250*, 1755. (d) Kirgan, R. A.; Sullivan, B. P.; Rillema, D. P. *Top. Curr. Chem.* **2007**, *281*, 45. (e) Vlcek, A., Jr. *Top. Organomet. Chem.* **2010**, *29*, 73.
(6) Chen, Y.-L.; Lee, S.-W.; Chi, Y.; Hwang, K.-C.; Kumar, S. B.; Hu, Y.-H.; Cheng, Y.-M.; Chou, P.-T.; Peng, S.-M.; Lee, G.-H.; Yeh, S.-J.; Chen, C.-T. *Inorg. Chem.* **2005**, *44*, 4287.
(7) (a) Ziessel, R. *J. Am. Chem. Soc.* **1993**, *115*, 118. (b) Feng, M.; Chan, K. S. *Organometallics* **2002**, *21*, 2743. (c) Chin, C. S.; Eum, M.-S.; Kim, S. Y.; Kim, C.; Kang, S. K. *Eur. J. Inorg. Chem.* **2007**, 372. (d) Ammermann, S.; Daniliuc, C.; Jones, P. G.; du Mont, W.-W.; Kowalsky, W.; Johannes, H.-H. *Dalton Trans.* **2008**, 4095.
(8) Lowry, M. S.; Bernhard, S. *Chem.—Eur. J.* **2006**, *12*, 7970.
(9) (a) Jiang, W.; Gao, Y.; Sun, Y.; Ding, F.; Xu, Y.; Bian, Z.; Li, F.; Bian, J.; Huang, C. *Inorg. Chem.* **2010**, *49*, 3252. (b) King, K. A.; Watts, R. J. *J. Am. Chem. Soc.* **1987**, *109*, 1589.
(10) Bedford, R. B.; Castillon, S.; Chaloner, P. A.; Claver, C.; Fernandez, E.; Hitchcock, P. B.; Ruiz, A. *Organometallics* **1996**, *15*, 3990.
(11) Lin, C.-H.; Chang, Y.-Y.; Hung, J.-Y.; Lin, C.-Y.; Chi, Y.; Chung, M.-W.; Lin, C.-L.; Chou, P.-T.; Lee, G.-H.; Chang, C.-H.; Lin, W.-C. *Angew. Chem., Int. Ed.* **2011**, *50*, 3182.
(12) Chou, P.-T.; Yu, W.-S.; Cheng, Y.-M.; Pu, S.-C.; Yu, Y.-C.; Lin, Y.-C.; Huang, C.-H.; Chen, C.-T. *J. Phys. Chem. A* **2004**, *108*, 6487.
(13) (a) Lee, C.; Yang, W.; Parr, R. G. *Phys. Rev. B* **1988**, *37*, 785. (b) Becke, A. D. *J. Chem. Phys.* **1993**, *98*, 5648.
(14) (a) Hay, P. J.; Wadt, W. R. *J. Chem. Phys.* **1985**, *82*, 270. (b) Hay, P. J.; Wadt, W. R. *J. Chem. Phys.* **1985**, *82*, 284. (c) Hay, P. J.; Wadt, W. R. *J. Chem. Phys.* **1985**, *82*, 299.
(15) Hariharan, P. C.; Pople, J. A. *Mol. Phys.* **1974**, *27*, 209.
(16) (a) Jamorski, C.; Casida, M. E.; Salahub, D. R. *J. Chem. Phys.* **1996**, *104*, 5134. (b) Petersilka, M.; Grossmann, U. J.; Gross, E. K. U. *Phys. Rev. Lett.* **1996**, *76*, 1212. (c) Bauernschmitt, R.; Ahlrichs, R.; Hennrich, F. H.; Kappes, M. M. *J. Am. Chem. Soc.* **1998**, *120*, 5052. (d) Casida, M. E. *J. Chem. Phys.* **1998**, *108*, 4439. (e) Stratmann, R. E.; Scuseria, G. E.; Frisch, M. J. *J. Chem. Phys.* **1998**, *109*, 8218.
(17) Cancès, M. T.; Mennucci, B.; Tomasi, J. *J. Chem. Phys.* **1997**, *107*, 3032.
(18) *Gaussian 03*, revision C.02; Gaussian, Inc.: Wallingford, CT, 2004.
(19) (a) Hung, J.-Y.; Chi, Y.; Pai, I.-H.; Cheng, Y.-M.; Yu, Y.-C.; Lee, G.-H.; Chou, P.-T.; Wong, K.-T.; Chen, C.-C.; Wu, C.-C. *Dalton Trans.* **2009**, 6472. (b) Hung, J.-Y.; Lin, C.-H.; Chi, Y.; Chung, M.-W.; Chen, Y.-J.; Lee, G.-H.; Chou, P.-T.; Chen, C.-C.; Wu, C.-C. *J. Mater. Chem.* **2010**, *20*, 7682. (c) Du, B.-S.; Lin, C.-H.; Chi, Y.; Hung, J.-Y.; Chung, M.-W.; Lin, T.-Y.; Lee, G.-H.; Wong, K.-T.; Chou, P.-T.; Hung, W.-Y.; Chiu, H.-C. *Inorg. Chem.* **2010**, *49*, 8713.
(20) Lin, C.-H.; Chi, Y.; Chung, M.-W.; Chen, Y.-J.; Wang, K.-W.; Lee, G.-H.; Chou, P.-T.; Hung, W.-Y.; Chiu, H.-C. *Dalton Trans.* **2011**, *40*, 1132.
(21) (a) Chen, K.-S.; Liu, W.-H.; Wang, Y.-H.; Lai, C.-H.; Chou, P.-T.; Lee, G.-H.; Chen, K.; Chen, H.-Y.; Chi, Y.; Tung, F.-C. *Adv. Funct. Mater.* **2007**, *17*, 2964. (b) Chen, B.-S.; Chen, K.; Hong, Y.-H.; Liu, W.-H.; Li, T.-H.; Lai, C.-H.; Chou, P.-T.; Chi, Y.; Lee, G.-H. *Chem. Commun.* **2009**, 5844. (c) Shen, X.; Yang, H.; Hu, X.-H.; Xu, Y.; Wang, F.-L.; Chen, S.; Zhu, D.-R. *Inorg. Chem. Commun.* **2009**, *12*, 785. (d) Ibers, J. A.; Hamilton, D. S.; Baddley, W. H. *Inorg. Chem.* **1973**, *12*, 229.
(22) (a) Caspar, J. V.; Meyer, T. J. *J. Phys. Chem.* **1983**, *87*, 952. (b) Kober, E. M.; Caspar, J. V.; Lumpkin, R. S.; Meyer, T. J. *J. Phys. Chem.* **1986**, *90*, 3722. (c) Treadway, J. A.; Loeb, B.; Lopez, R.; Anderson, P. A.; Keene, F. R.; Meyer, T. J. *Inorg. Chem.* **1996**, *35*, 2242.(d) Yersin, H. *Highly Efficient OLEDs with Phosphorescent Materials*; Wiley-VCH: Weinheim, Germany, 2008. (e) Chou, P.-T.; Chi, Y.; Chung, M.-W.; Lin, C.-C. *Coord. Chem. Rev.* **2011**, doi:10.1016/j.ccr.2010.12.013.
(23) Chen, K.-Y.; Hsieh, C.-C.; Cheng, Y.-M.; Lai, C.-H.; Chou P.-T.; Chow, T. J. *J. Phys. Chem. A* **2006**, *110*, 12136.
(24) (a) Su, S.-J.; Chiba, T.; Takeda, T.; Kido, J. *Adv. Mater.* **2008**, *20*, 2125. (b) Hung, W.-Y.; Ke, T.-H.; Lin, Y.-T.; Wu, C.-C.; Hung, T.-H.; Chao, T.-C.; Wong, K.-T.; Wu, C.-I. *Appl. Phys. Lett.* **2006**, *88*, 064102. (c) Naka, S.; Okada, H.; Onnagawa, H.; Tsutsui, T. *Appl. Phys. Lett.* **2000**, *76*, 197. (d) Wu, S.-H.; Li, W.-L.; Chu, B.; Lee, C. S.; Su, Z.-S.; Wang, J.-B.; Ren, Q.-J.; Hu, Z.-Z.; Zhang, Z.-Q. *Appl. Phys. Lett.* **2010**, *96*, 093304. (e) Sasabe, H.; Gonmori, E.; Chiba, T.; Li, Y.-J.; Tanaka, D.; Su, S.-J.; Takeda, T.; Pu, Y.-J.; Nakayama, K.; Kido, J. *Chem. Mater.* **2008**, *20*, 5951. (f) Kido, J.; Ohtaki, C.; Hongawa, K.; Okuyama, K.; Nagai, K. *Jpn. J. Appl. Phys.* **1993**, *32*, 917.
(25) Strohriegl, P.; Grazulevicius, J. V. *Adv. Mater.* **2002**, *14*, 1439.
(26) Adachi, C.; Baldo, M. A.; Forrest, S. R. *J. Appl. Phys.* **2000**, *87*, 8055.
(27) Aziz, H.; Popovic, Z. D. *Appl. Phys. Lett.* **2002**, *80*, 2180.
(28) (a) Holmes, R. J.; D'Andrade, B. W.; Forrest, S. R.; Ren, X.; Li, J.; Thompson, M. E. *Appl. Phys. Lett.* **2003**, *83*, 3818. (b) Ren, X.; Li, J.; Holmes, R. J.; Djurovich, P. I.; Forrest, S. R.; Thompson, M. E. *Chem. Mater.* **2004**, *16*, 4743.